Observation of Preferential Pathways for Oxygen Removal through Porous Transport Layers of Polymer Electrolyte Water Electrolyzers

Pongsarun Satjaritanun[a,+], Maeve O'Brien[b,+], Devashish Kulkarni[b], Sirivatch Shimpalee[c], Cristopher Capuano[d], Katherine E. Ayers[d], Nemanja Danilovic[e], Dilworth Y. Parkinson[e] and Iryna V. Zenyuk[a,b*]

[a]Department of Chemical and Biomolecular Engineering; National Fuel Cell Research Center, University of California Irvine, Irvine, CA, USA

[b]Department of Material Science and Engineering, University of California Irvine, Irvine, CA, USA

[c]Department of Chemical Engineering, University of South Carolina, Columbia, SC, USA

[d]Nel Hydrogen, Wallingford, CT, USA

[e]Lawrence Berkeley National Laboratory, Berkeley, CA, USA

[+]Contributed equally

[*]Corresponding author: Iryna.zenyuk@uci.edu

Lead Contact: Iryna Zenyuk, Iryna.zenyuk@uci.edu

SUMMARY

Understanding the relationships between porous transport layer (PTL) morphology and oxygen removal is essential to improve the polymer electrolyte water electrolyzer (PEWE) performance. *Operando* x-ray computed tomography and machine learning were performed on a model electrolyzer at different water flowrates and current densities to determine how these operating conditions alter oxygen transport in the PTLs. We report a direct observation of

oxygen taking preferential pathways through the PTL regardless of the water flowrate or current density (1- 4 A/cm^2). Oxygen distribution in the PTL had a periodic behavior with period of 400 μm. Computational fluid dynamics model was used to predict oxygen distribution in the PTL showing periodic oxygen front. Observed oxygen distribution is due to low in-plane PTL tortuosity and high porosity enabling merging of oxygen bubbles in the middle of the PTL and also due to aerophobicity of the layer.

KEY-WORDS:

Porous Transport Layer, X-ray CT, Electrolyzer, Oxygen transport, Lattice-Boltzmann simulations

INTRODUCTION

The polymer electrolyte water electrolyzer (PEWE) is an essential part of a renewable energy economy. It uses renewable electricity to convert water into oxygen and hydrogen (Carmo et al., 2013). The product of interest from water electrolysis is hydrogen, a fuel that can be easily stored as compressed gas, transported via natural gas pipelines, and then combusted as a fuel or converted back to electricity in polymer electrolyte membrane (PEM) fuel cells. The produced hydrogen gas has a specific energy density of 120 MJ/kg, whereas gasoline has a specific energy density of 44 MJ/kg; this difference in specific energy density values is what makes hydrogen an attractive alternative fuel, as hydrogen has approximately 2.7 times the amount of energy per kilogram than liquid gasoline (Mazloomi and Gomes, 2012). Although

water electrolysis is a well-established method for producing hydrogen, there remain several knowledge gaps to maximize efficiency in converting water to hydrogen and oxygen while minimizing production cost (Babic et al., 2017).

The overall electrochemical water splitting is divided into two half-cell reactions. When a potential is applied across PEWE, an oxygen evolution reaction (OER) occurs on the anode and a hydrogen evolution reaction (HER) occurs on the cathode of the electrolyzer (Wang et al., 2019). For the OER, water flows in via the anode and transports through the porous transport layer (PTL) to reach the catalyst layer (CL). Once in contact with the electrocatalyst, two moles of water are split into four protons, four electrons, and one mole of oxygen gas. Byproduct oxygen exists the PEWE either as dissolved oxygen or in a gas phase. Residual oxygen bubbles can prove to be problematic during the operation of an electrolyzer, as it can block water from reacting with the electrocatalyst, thus decreasing the overall electrolyzer efficiency. Figure 1 shows a schematic of transport processes within PEWE. Particularly at high current densities, the mass transport losses are mainly caused by inefficient removal of oxygen from the electrolyzer (Suermann et al., 2015). In order to enhance the mass transport, the mechanisms of oxygen transport in the PTL need to fully be understood.

As an effort to better understand the two-phase transport behavior in the PTL, studies (Abdin et al., 2015; Dedigama et al., 2014; García-Valverde et al., 2012; Han et al., 2016; Kadyk et al., 2016; Kang et al., 2018, 2017; Kim et al., 2020; C. Lee et al., 2020; Lee et al., 2017; Leonard et al., 2020, 2018; Lopata et al., 2020; Schuler et al., 2019; Seweryn et al., 2016; Suermann et al., 2017; Zlobinski et al., 2020) have focused on using imaging techniques to investigate the evolution and transport of oxygen in electrolyzers; including optical, neutron or x-

ray imaging as well as computational studies. Optical microscopy was utilized by Dedigama et al. (Dedigama et al., 2014) in order to study two-phase flow in an operating electrolyzer. With a 7,000 fps camera, as well as a transparent sheet and specific backlighting, they were able to capture anodic two-phase behavior with high temporal accuracy. Following this study, Lee et al. (Lee et al., 2017) employed a microfluidic platform, termed PTL-on-Chip, to study the effect of microstructure on the growth of oxygen bubbles, using an optical microscope. It was concluded that the morphology of the PTL has a significant impact on the governing force of the oxygen gas cluster growth and dictates the flow regime during PEWE operation.

Neutron radiography has been utilized by Seweryn et al. (Seweryn et al., 2016) to visualize steady-state oxygen distribution in the PTLs. They were able to observe oxygen residence time in a PTL, specifically porous titanium (Ti), and shown an equilibrium in the two-phase flow in the PTL. Their observations surprising at a time, suggested that the PTL would always be saturated with water, regardless of the current density and that oxygen saturation did not change with current density in the regime of 0.1 – 2.5 A/cm^2. Lee et al. (C. Lee et al., 2020) have investigated the dynamic gas transport behavior in the anode PTL by using *operando* synchrotron x-ray imaging. When they applied the current with a steep ramp-up and a shallow ramp-down. They concluded that the oxygen responds more rapid, which means that the gas saturation in the PTL reached steady state quickly. Zlobinski et al. (Zlobinski et al., 2020) have studied the effect of the two-phase flow behavior within PTLs under steady-state and dynamic load of the electrolyzer by using a neutron imaging using high spatial resolution (6 μm) and relatively high temporal resolution (1 s exposure time). They concluded that the two-phase flow in PTLs is purely capillary driven for a wide range of operating conditions and that viscous

forces are negligible. They further confirmed the findings of Seweryn et al. that water and gas distribution is not affected by current density (from 10 to 2000 mA/cm^2). Leonard et al. (Leonard et al., 2020, 2018) were able to observe oxygen bubble formation and transport with x-ray CT and radiography using *operando* hardware. This work demonstrated that as the current density increased, the residence time of oxygen bubbles in the channel decreased; this was expected, as higher current density would result in more oxygen being formed, enabling faster oxygen bubbles detachment. With Ti PTLs currently it is experimentally not possible to differentiate between water and oxygen in the PTL, as Ti is highly x-ray attenuating material. Therefore, limited information is known on microscale distribution of oxygen in the PTL, and how PTL morphology can be tailored to remove oxygen more effectively, as the in-plane vs through-plane transport properties can be rationally designed.

The aim of this work is to investigate oxygen content in the PTLs and its relation to both PEWE current density and water flow rate, as well as understand whether oxygen takes preferential pathways when transporting through the PTL. To that end, a PEWE was set up with a model treated carbon fiber PTL (with similar morphological properties to Ti PTL) in order to directly observe and quantify both the oxygen content and preferential pathways oxygen could take as it exits PTL using *operando* x-ray CT. Using carbon-fiber PTLs and short experimental imaging time enables direct observation of the steady-state pathways for oxygen transport within the carbon PTL. This is unprecedented, as no previous study has seen the pore-scale observation of oxygen content within the PTL with *operando* techniques. In order to distinguish oxygen within the PTL, machine learning was utilized to analyze the amount of oxygen present in the PTL of the electrolyzers at varying flow rates and current densities. The direct three-dimensional

model-based Lattice Boltzmann Method (LBM) was used to better understand the physics behind the two-phase transport in the PTL under different cell operating conditions.

EXPERIMENTAL

X-ray computed tomography (CT)

X-ray CT was conducted at the Advanced Light Source (ALS), on beamline 8.3.2, at the Lawrence Berkeley National Laboratory (LBNL). The optics used were as follows: 50 μm LuAg: Ce scintillator, 5x lenses, a sCMOS PCO Edge camera, and a double multilayer monochromator. The x-ray energy selected was 26 keV. The resulting images had a voxel resolution of 1.3 μm and a horizontal field of view (FOV) of 3.3 mm. The x-ray CT images required sample rotation (180-degrees), and therefore special care had to be taken so that the water inlet and gas outlets, as well as the thermocouples, did not become tangled. These parameters resulted in a scan time of ~6 minutes.

Materials

The catalyst coated membranes (CCMs) used in this experiment were provided by NEL Hydrogen, Wallingford, CT, and consisted of CCMs with catalyst loadings of 3 mg/cm^2 of platinum (Pt) on the cathode and 3 mg/cm^2 of iridium oxide (IrOx) on the anode. Nafion 117 was used as a PEM. The PTLs that used were treated and untreated Freudenberg carbon paper (Fuel Cell Store, College Station, TX) without MPL, for anode and cathode respectively. Treatment was done in piranha solution for five hours to make the PTL surface hydrophilic. The piranha solution treatment resulted in irreversible wettability modification, where the contact angle of the PTL was reduced from 133±4 degrees to about 0 degrees. The PTLs completely took in water,

indicating the completely hydrophilic surfaces. Furthermore, the PTLs hydrophilicity was also confirmed with x-ray imaging as will be discussed later. Two Freudenberg GDLs with 50 % compression on the anode side were used to simulate morphology of the Ti PTLs. The compressed GDLs should have pore sizes of less than 10 μm in diameter, which is what the typical pore sizes for sintered Ti PTLs. In this study, treated Freudenberg at this compression has pore sizes comparable to conventional PTL, which has the average pore size about 10 μm in diameter, as reported in Supplementary Information (SI), Figures S1 and S2. The main morphological difference between the carbon-fiber PTL used in this study and Ti-based PTL is the different through-plane vs. in-plane tortuosities. The PTL studied here has in-plane tortuosity of 1.3 (Figure S1D), whereas Ti PTL has in-plane tortuosity of 3.3 – 3.9 (Leonard et al., 2020). The cathode had untreated Freudenberg GDL. The anode and cathode bipolar plates (BPPs) were made of graphite, as operating time of electrolyzers was only several hours and therefore low corrosion currents were observed from using carbon PTL and carbon bipolar plates. Our earlier study proved that it is possible to operate PEWE with carbon PTLs for short duration without significant carbon corrosion (Leonard et al., 2018). Furthermore, recent benchmarking study across leading PEWE laboratories in the world also used carbon layer instead of Ti for PTL to conduct the benchmarking round robin study (Bender et al., 2019).

RESULTS AND DISCUSSION

Interpreting tomography data

Figure 1 shows the 3D volume rendering and the cross-section tomographs for the PEWE configuration. The 3D volume rendering displays the composition and morphology of the PEWE, as shown in Figure 1A. At the anode side, water was transported from the channel to the catalyst layer and the oxygen product was removed from the catalyst layer. It is difficult to quantify

oxygen content in the PTL by using only 3D visualization. The cross-section tomographs were created for ease of visualization and quantification. The relevant planes examined in this study are labeled and highlighted in Figure 1.

The y-z plane is used to understand how the oxygen content changed within the length of the PTL, as shown in Figure 1B. By area-averaging information in the y-z plane, oxygen content under land versus that under channel was found. It is used mostly to quantify land-channel effects on oxygen distribution. The x-y plane is the through-plane view where one can observe both channels, the land, the cathode GDL, the PE membrane, the catalyst layer, and the anode PTL in the same slice, as shown in Figure 1C. A tomograph 'slice' is essentially a single reconstructed image that is used to build up the 3D data. This front-facing slice was used to determine the oxygen content along the length of the anode-side PTL. The brightest spots near both sides of the PEM are the catalyst layers. This is due to the high x-ray attenuation of the catalyst materials (Ir and Pt) making them very distinguishable. At the x-z plane, oxygen appears as dark, as it has the lowest x-ray attenuation on the anode side, as shown in Figure 1D. Water and carbon have comparable x-ray attenuation, so it is difficult to render them separately, therefore a single phase will be used to identify both in this study. The x-z plane, which is the in-plane or top-down view, was used to train the Weka machine learning algorithm in order to interpret the oxygen content throughout the PTL. In addition to using the x-z plane for interpreting the oxygen content in the PTL, it was also used with the z-project function in ImageJ to build an average of the amount of oxygen and the catalyst distribution.

The x-ray CT scan of an electrolyzer under OCV condition was performed to observe whether there any residual oxygen trapped within the electrolyzer. Figure S5 compares a cross-

section image of an identical location of electrolyzer at the OCV and that at 1 A/cm^2, where all the PTL is filled with water. This image proves that piranha solution treatment of PTLs was successful and the PTL is mostly hydrophilic. From this figure, one can observe that the PTL under the land is more compressed than under the channel. This is to be expected, as the PTL was compressed by 50 % to achieve pore sizes comparable to those of Ti PTLs. The cathode PTL shows a lower degree of compression than cathode as expected given the target of 20 % compression on the cathode.

Oxygen Transport Pathways Under Various Current Densities

Observing oxygen transport pathways is an important step towards understanding the transport of evolved oxygen and supplied water through the PTL. Figure 2 shows the x-y plane of the PEWE during cell operation at 1A/cm^2 and 4 A/cm^2 with varied flowrates of water. The electrochemical data showing stable potentials at these current densities is shown in Figure S6, and overall polarization curves by Figure S7 at three water flowrates. The tomography cross-sections were selected as representative of the whole domain and they reveal that the oxygen pathways are visible within the PTL. Figures 2A-C present the x-y plane of cell that operates at 1 A/cm^2 with the flow rates of 1 mlpm to 3 mlpm, respectively. False coloring on these cross-sections provided an example of the oxygen transport pathways in the PTL. The result shows that oxygen content in the PTL did not change as water flow rate increased from 1 to 3 mlpm. There are several locations where oxygen goes all the way through from the catalyst layer to the channel or land. However, there are some locations showing that the oxygen is trapped in the PTL under the land area. Similar to Leonard et al. (Leonard et al., 2020), there is a more gas observed under the land areas. Comparing Figures 2A-C at 1 A/cm^2 to Figure S5 at OCV, there

are a significant amount of oxygen present in the PTL after the current density is applied compared to that at OCV, which will be quantified in the later sections.

Figures 2D-F show the x-y cross-section tomographs of the PEWE that operates at 4 A/cm^2 with the flow rates of 1 mlpm to 3 mlpm, respectively. Comparing these operating conditions to 1 A/cm^2 at all flow rates, these figures appear virtually identical, although current densities are four times higher for Figures 2E-F compared to Figures 2A-C. Oxygen seems to follow the same pathways at 4 A/cm^2 as at 1 A/cm^2. No new pathways emerged for oxygen removal. The oxygen content for PEWE operating at 2 A/cm^2 and 3 A/cm^2 is shown in Figure S8. Although these images are only 2D cross-sections, the oxygen transport seem to follow the same pathways through the PTL, regardless of current density or water flow rate for the range studied.

Impact of current density and flow rate on oxygen transport in PTL

Oxygen bubbles may accumulate and become trapped in the pore space of the PTL, resulting in mass transport losses. Figure 3 shows averaged oxygen content within the PTL as a function of the PTL thickness. The PTL/catalyst layer interface is located at x = 0 whereas the flow field is located at x = 320 μm. The oxygen content in the channel is uncertain due to difficulty to quantify oxygen content within the interface of PTL and channel/land, showing no obvious trend among flow rates, yet this does not significantly impact the computed oxygen content in the PTL, especially near the catalyst layer. Figure 3A shows the comparison of oxygen content for 1 A/cm^2 at different flow rates. The oxygen content near the catalyst layer is between 30 and 40 %. Then, in the middle of PTL, it decreases to about 15%, and near the channel it varies with flow rate. For the cell measurements at 1 A/cm^2, the cell was not fully conditioned, so

more oxygen near the catalyst layer was observed, compared to operation at higher current densities. At 4 A/cm^2, oxygen content near the catalyst layer was 20-30 % and it decreased to 5 % near the flow field, after which it increased again when entering the channel, as shown in Figure 3B. The results for the other cell operating conditions were reported in Figure S9. From the overall measurement of oxygen content as a function of PTL thickness, the results show that there is a high oxygen content at the catalyst layer interface with the PTL. Gas transport pathways merge approaching the middle of the PTL. As mentioned above, some of the oxygen is trapped in the PTL near the land area but due to low in-plane tortuosity (shown by SI, Figure S1) for this type of PTL the majority of oxygen is laterally removed from under the land into the channel.

Figure 3C shows the oxygen content comparison with varied currents at the same flow rate of 2 mlpm. Again, there seems to be no correlation between current density and oxygen content within the PTL. Zlobinski et al. (Zlobinski et al., 2020) and Seweryn et al. (Seweryn et al., 2016) were able to quantify water saturation in the PTL via neutron radiography. Zlobinski et al. confirmed the earlier Seweryn et al. study that oxygen content in PTLs did not change with current density from 0.1 to 2 A/cm^2. They showed that near the catalyst layer, the water and oxygen saturations were 0.5. In this study, oxygen content which is equivalent to oxygen saturation is approximately 0.2 to 0.4 near the catalyst layer. Oxygen content near the flow field is close to 0, in agreement with Zlobinski et al. Note that their PTL thickness is 1 mm, about 3 times higher than that used in our study, which increases the transport pathlength and leads to more oxygen accumulation near the catalyst layer. In Lee et al. 250 μm PTL was used in neutron

radiography study (C. H. Lee et al., 2020) and they observed ~0.3 oxygen saturation near catalyst layer, which is close to the value obtained in this study.

Oxygen Transport Classification in Various Regions of the PTL

To better understand oxygen transport in the PTL, oxygen content within the three through-thickness portions of the PTL was investigated. Figure 4 shows the comparison of oxygen content distribution within the PTL at 1 A/cm^2 with the flow rate of 2 mlpm. The PTL was separated into three portions: near the catalyst layer interface (CL/PTL), middle of PTL (Mid PTL), and near the land/channel interface (PTL/Channel), as shown at the top of Figure 4A. The through-plane view of oxygen content generated with the z-project (averaged from 3D volume and projected onto a single slice) is depicted in Figure 4A, where the volumetric information of oxygen content in the PTL was combined into a single image.

Figures 4C-E show the in-plane view of oxygen content in the portions of catalyst layer/PTL, Mid PTL, and PTL/Channel, respectively. The location near the catalyst layer shows that the local oxygen content can be as high as 70 % in certain locations, mainly under the land, however on average as shown in Figure 3, it is below 40 %. The oxygen content gradually decreases when transporting through the mid-PTL and PTL/channel, respectively. The oxygen content of each portion was measured along the length of the sample and plotted, as shown in Figure 4B. The average oxygen content in each PTL portion from catalyst layer/PTL to PTL/Channel was 35.7%, 18.8%, and 7.1%, respectively. Thus, it roughly halved as oxygen transported through each of the 1/3 sections of the PTL. The results show that the distribution of oxygen content seems to be a “spatially periodic front”, especially at the Mid-PTL and PTL/Channel portions. The spatial pattern is parallel to the land-channel location and is in the

same direction of water flow. The oxygen peaks appear every 400 μm, where the oxygen peaks vary from 12 to 25 %, whereas the oxygen content valleys (water-rich locations), vary from 2.5 to 7 %.

Figure 5 presents the oxygen content comparison in the three portions of the PTL for the PEWE operating at 4 A/cm^2 with the water flowrate of 2 mlpm. The result shows that the average oxygen content in each PTL portion from CL/PTL to PTL/Channel is 27.5 %, 18.4 %, and 7.5 %, respectively, as shown in Figure 5B. These values are slightly lower than the ones observed for operation at 1 A/cm^2. As explained before, at 1 A/cm^2 the CCM was most likely not fully conditioned well, not reaching its full steady state. Peaks in the oxygen content are observed below the land regions, similar to the case of 1 A/cm^2, indicating that some oxygen was trapped under the land. Figures S10 and S11 show oxygen content within three selected regions for PEWE operating at 2 and 3 A/cm^2 and water flow-rate of 2 mlpm, showing very similar distributions to Figure 4 and Figure 5, confirming that the oxygen prefers the same transport pathways through the PTL, regardless of current density. And Figure S12 compares oxygen distributions across current densities and flowrates.

The spatially periodic oxygen front observed here for all the current densities has not been reported before. We provide several hypotheses to explain its physics, which we will attempt to prove or disprove: 1) oxygen periodic front is due to catalyst layer inhomogeneous distribution, 2) electrochemical decoupling of catalyst sites due to local oxygen flooding at the catalyst sites, 3) interplay between in-plane/through-plane PTL morphology, wettability and resulting bubble coalescence and transport. Regarding hypothesis 1, we plotted catalyst layer distribution and correlated it to the oxygen waveform. Figure S13 shows a map of catalyst

distribution. There was little to no correlation found between the catalyst distribution and the oxygen content, as correlation coefficients are below 0.1 (Figure S13C). Hypothesis 2 attempts to explain the periodicity in oxygen front with electrochemical decoupling of the catalyst sites. As when the oxygen locally saturates the catalyst layer, catalyst will not be active towards splitting water due to either proton limitations or unavailability of water vapor, however after oxygen diffuses away, the catalyst becomes active again. In general, within the catalyst layer, the IrOx is hydrophilic and it is likely that liquid water is present either within the ionomer or directly on the surface of the catalyst, if that is not the case, water can react in the vapor phase, as well (Fornaciari et al., 2020). There is no literature studies investigating the length-scale of these decoupling phenomena. In this study, the periodic oxygen front was found to be pronounced in the location of 160 μm, away from catalyst layer, which is a half of the PTL thickness, as shown in Figures 4A and 5A. Therefore this hypothesis is unlikely, however, we did perform additional model simulations with this options to be certain (see Figure S14 and S15 and discussion in SI). And these model simulations did not predict the experimentally observed oxygen wave front. Therefore, we believe it is transport and not kinetics that is responsible for the periodic oxygen front observation.

This periodicity is perhaps due to oxygen taking preferential pathways as it exits the PTL, which would account for the apparent periodicity, hypothesis 3. Zlobinski et al. (Zlobinski et al., 2020) suggests that the pore network inherent to a porous media- in their case it was sintered Ti PTL could account for the gas traps. Gas traps are areas of either high hydrophobicity or hydrophilicity inherent to a porous media. Since PTL was well treated and OCV data shows no hydrophobic locations within the PTL it is difficult to explain the periodicity with the gas traps.

Instead, we believe that the observed oxygen removal is due to different PTL in-plane vs through-plane tortuosities, 1.3 vs. 1.7, its wettability (completely aerophobic) and pore-size distribution. We explore the third hypothesis in more detail in the next section using multi-physic model.

Modeling of oxygen transport in PTL

Figure 6 shows the comparison of oxygen content in the PTL between the CFD simulation and the experimental data at 1 and 4 A/cm^2 having water flowrate of 2 mlpm. The CFD simulations were able to adequately predict oxygen content in the PTL having aerophobic pores (water contact angle of 10 degrees), especially in the middle and at the interface with the flow-field, as evidenced by the agreement of average oxygen content with experimental data (Figures 6C-D). The model overpredicts oxygen content near the catalyst layer by 10 %. Oxygen content in the PTL for 1 A/cm^2 and 4 A/cm^2 predicted by model is very similar and oxygen pathways do not change when current density is increased. The shape of the oxygen front is somewhat different, also periodic but with the period of 200 μm, which is half of that observed experimentally. Furthermore, the simulations reveal that more oxygen was trapped in the PTL under the land area, compared to the experimental observations.

To understand the differences between experimental and CFD data we need to better understand model assumptions, physics incorporated and its current limitations. These are listed in the SI but and we will focus on the most relevant assumptions here. Within the model, oxygen bubbles nucleate within the catalyst layer with the nucleation radius of 1 μm and nucleation site density of 1 site/μm. The exact location and density of the nucleation sites and bubble nucleation radius are not well-known, although other studies have assumed 1 nm nucleation radius (Kadyk

et al., 2016). Generally, oxygen is formed in dissolved form and nucleates over the hydrophobic defects, when the dissolved oxygen critical saturation concentration is reached. We cannot determine here from the experimental data whether oxygen bubble nucleation is uniform over the catalyst layer area due to the resolution limitation. Once the bubble nucleates its radius will grow to a critical size and it will detach from the nucleation site and the next bubble will nucleate and grow and the process will repeat. The radius of a bubble upon detachment depends on mechanical balance of forces, such as buoyancy, pressure, capillary, drag and lift. The shape and size of the bubble can be characterized by the Eotvos (Eo) number, which is correlated to gravity, g, density difference between fluids, $\Delta\rho$, and surface tension, σ:

$$Eo = \frac{\Delta\rho g b^2}{\sigma} \quad (2)$$

where, b is characteristic length scale taken to be mean size of the pores of the PTL of 10.3 μm in this work. The calculated Eo number was 1.36×10^{-4} and the parameters used for calculation are reported in Table S1. Eo << 1 indicates that the bubble transport is dominated by the surface tension and hence capillary forces are dominant, whereas gravity and buoyancy are minor driving forces. (Sattari et al., 2020) From here it is evident, that bubble shape and path of transport will be determined by PTL wettability and pore size distribution, as well, as current density (oxygen gas pressure). The pore size distribution of this PTL sample is shown in the SI Figure S1E.

The wettability of the PTL in this study is the following: it is hydrophilic and aerophobic. Oxygen first will displace water from the large hydrophilic pores and then from the small hydrophilic pores. If any hydrophobic pores are present then oxygen will first fill those before

advancing into the hydrophilic domains, however here we do not observe hydrophobic pores. The shape of the oxygen bubbles will always be concave, as water has convex menisci in the hydrophilic porous media. Thus, the bubble transport will be guided by the pore size distribution of the PTL, as shown by Figures 6E-F. Oxygen will nucleate and grow as bubbles at the surface of the catalyst layer, transport through the large pores of the PTL displacing water. The PTL selected here has good in-plane transport properties, and also large porosity in the middle of the PTL, as shown by Figure S2, therefore oxygen gas will merge and coalesce in-plane, as these are the pores of low resistance before finally transporting into the channel. The high-porosity band in the middle of the PTL is mainly due to two PTL layers stacked together in this study and it allows oxygen to merge and to form a periodic waveform. Note that the PTL does not have porosity that replicates oxygen pattern here. Once the pathway is established for oxygen removal, the energy it takes for oxygen to form a new pathway is much higher than that for it to take the established pathway. The flux of oxygen will be higher at higher current densities but the oxygen pathways remain the same. Therefore, the morphology of the PTL determines the expulsion pathways through which oxygen travels. As discussed above, the model physics do not currently capture the nucleation and growth of bubbles at the catalyst layer surface effectively and we believe this causes the deviation between the modeling and experimental results. This study is also performed with a CFD simulation with a uniform flux of oxygen and a PTL that is aerophilic (water contact angle of 170 degrees), as shown in Figures S16 and S17. The simulations show that the oxygen transport pathways did not change from 1 to 4 A/cm^2 and no periodicity in oxygen removal was observed. Additionally, we explored the PTL contact angle of 10 and 50 degrees as shown by Figure S18, indicating that oxygen content in PTL does not change significantly when contact angle increased to 50 degrees.

Existing commercial PTLs, such as sintered or fiber PTLs have uniform morphology and pore-size distribution through the thickness of the PTL(Leonard et al., 2020). These PTLs also have lower through-thickness vs. in-plane tortuosities, essentially eliminating the possibility of oxygen front merging in-plane in the middle of the PTL. The periodic waveform in this study also enables effective water delivery to the catalyst sites. Good in-plane transport properties, as shown in this study can eliminate oxygen accumulation under the lands. It is possible to tailor the Ti-based PTL morphology to enable better in-plane transport by introducing gradient in particle sizes through the thickness of the PTL, or using the fiber-based Ti PTLs and stacking two thinner layers instead of one thicker, although PTL-PTL contact resistances have to be accounted for.

CONCLUSIONS

In this study, x-ray CT and CFD were used to investigate oxygen transport in the PTLs of PEWE. This study aimed to explain the preferential pathways of oxygen transport through the PTL. X-ray CT was performed using the in-house designed electrolyzer at different water feed rates (1- 3 mlpm) and current densities (1 - 4 A/cm^2). Here, an acid-treated Freudenberg GDL was used as a model PTL on the anode because its pore size distribution most closely resembles conventional Ti-based sintered or fiber PTLs. Weka machine learning incorporated with the Z project method was able to quantify oxygen content throughout the PTLs via post-processing of *operando* x-ray CT scans.

The results show that more oxygen was present in the PTL near the catalyst layer (~27.5 %), compared to near the flow field (~7.5 %). Oxygen content in the PTL varied very little with either flow rate or current density, within the studied range. In addition, the oxygen content exhibited spatial periodicity, with peaks appearing at approximately 400 μm. These peaks range

from 12 % oxygen content to a height of 25 % oxygen content. These findings are novel, as this is the first-time oxygen content has been directly observed and quantified on a pore-scale with direct observations.

While CFD correctly predicted overall average oxygen content within the PTL, it showed a periodic trend of oxygen wave form with a period of 200 μm a deviation between the model and experiment results we believe is due to current limitations in implementation of bubble nucleation and growth within the CFD model. Overall, oxygen transport in this hydrophilic/aerophobic PTL is guided by pore size distribution of the PTL. Oxygen will transport through the large voids first before filling smaller voids. Thus, once the pathway through the thickness of the PTL is established, oxygen bubbles will preferentially follow the pathway and no new pathways will be introduced within the current densities range studied here. The high in-plane transport properties of the PTL (tortuosity of 1.3) compared to the through-plane (tortuosity of 1.8) enable oxygen to merge in the middle of the PTL and form the waveform. This periodic waveform has not been previously observed, and we believe this is due to the fact that commercial Ti PTLs have better through-plane than in-plane transport properties and thus merging of the oxygen pathways will not occur.

Since oxygen tends to take preferential pathways through the PTL, one can rationally design PTL for selective water transport in and oxygen removal out. This can be achieved by either tailoring pore sizes or wettability. Hydrophobic PTL patterning will enable oxygen transport from the PTL at low resistance, however, water transport will be impeded. Gradient in porosity (Lettenmeier et al., 2017) in hydrophilic PTL can direct oxygen transport, as oxygen will transport along the large voids. If microporous layers (MPL) are to be designed (Schuler et

al., 2020), we believe introduction of cracks into the MPL can help with oxygen removal. Similar to this study, providing a high-porosity band in the middle of PTL can help merge oxygen bubbles into a single channel, minimizing the area of PTL for oxygen removal and providing more area within the PTL for water transport. The solutions suggested here can be expensive and will improve mass transport at high current densities (> 2 A/cm^2). The voltage gains due to improved PTL transport properties have to be assessed with respect to the cost of production of advanced PTLs.

Limitations of the Study

Our work has demonstrated new findings in oxygen transport behavior in porous transport layers of polymer electrolyte water electrolyzers by using *operando* x-ray CT in combination with the LBM simulation. The spatially periodic oxygen front has been observed in this study for the first time. The study was applied to a single type model PTL. Additional investigations are needed to generalize the findings and to ensure that these are translatable across the families of the PTLs. Future modeling study needs to incorporate the temperature effects and electrochemical kinetics to better capture transport effects on the oxygen transport behavior inside the PTLs.

Resource Availability

Lead Contact

Further information and requests for resources should be directed to and will be fulfilled by the Lead Contact, Iryna V. Zenyuk (Iryna.zenyuk@uci.edu).

Materials Availability

This study did not use or generate any reagents.

Data and Code Availability

This published article includes all datasets generated or analyzed during this study. The imaging data that support the figures and plots in this work are available from the lead contact upon reasonable request.

METHODS

All methods can be found in the accompanying Transparent Methods supplemental file.

SUPPLEMENTAL INFORMATION

Supplemental Information can be found online at DOI:

ACKNOWLEDGEMENT

Authors would like to acknowledge funding from the HydroGEN Advanced Water Splitting Materials Consortium, established as part of the Energy Materials Network under the U.S. Department of Energy, Office of Energy Efficiency and Renewable Energy, Fuel Cell Technologies Office and program managers David Peterson and Katie Randolph. This work was supported by DOE EERE award number EE0008081.The Advanced Light Source is supported by the Director, Office of Science, Office of Basic Energy Sciences, of the U.S. Department of Energy under Contract No. DE-AC02-05CH11231. The authors would like to acknowledge Dassault Systèmes Simulia S.L.U. for providing the XFlow software.

AUTHOR CONTRIBUTIONS

P.S., M.O'B., and I.V.Z. analyzed the data and prepared the manuscript. D.K. and I.V.Z. designed the operando hardware and experiments. M.O'B. and I.V.Z. carried out all the experiments. D.Y.P. helped set-up experiments and x-ray CT beamline. P.S. and S.S. designed and carried out the modeling study. C. C., K.E.A., N. D. and I.V.Z. defined the experimental approach and supervised. All authors contributed to the discussion and analysis of the data, as well as the editing of the manuscript.

DECLARATION OF INTERESTS

The authors declare no competing interests.

References

Abdin, Z., Webb, C.J., and Gray, E.M. (2015). Modelling and simulation of a proton exchange membrane (PEM) electrolyser cell. Int. J. Hydrogen Energy 40, 13243–13257.

Babic, U., Suermann, M., Büchi, F.N., Gubler, L., and Schmidt, T.J. (2017). Critical Review—Identifying Critical Gaps for Polymer Electrolyte Water Electrolysis Development. J. Electrochem. Soc. 164, F387–F399.

Bender, G., Carmo, M., Smolinka, T., Gago, A., Danilovic, N., Mueller, M., Ganci, F., Fallisch, A., Lettenmeier, P., Friedrich, K.A., Ayers, K., Pivovar, B., Mergel, J., and Stolten, D. (2019). Initial approaches in benchmarking and round robin testing for proton exchange membrane water electrolyzers. Int. J. Hydrogen Energy 44, 9174–9187.

Carmo, M., Fritz, D.L., Mergel, J., and Stolten, D. (2013). A comprehensive review on PEM water electrolysis. Int. J. Hydrogen Energy 38, 4901–4934.

Dedigama, I., Angeli, P., Ayers, K., Robinson, J.B., Shearing, P.R., Tsaoulidis, D., ans Brett,

D.J.L. (2014). In situ diagnostic techniques for characterisation of polymer electrolyte membrane water electrolysers - Flow visualisation and electrochemical impedance spectroscopy. Int. J. Hydrogen Energy 39, 4468–4482.

Fornaciari, J.C., Gerhardt, M.R., Zhou, J., Regmi, Y.N., Danilovic, N., Bell, A.T., and Weber, A.Z. (2020). The Role of Water in Vapor-fed Proton-Exchange-Membrane Electrolysis. J. Electrochem. Soc. https://doi.org/10.1149/1945-7111/ab9b09

García-Valverde, R., Espinosa, N., and Urbina, A. (2012). Simple PEM water electrolyser model and experimental validation. Int. J. Hydrogen Energy 37, 1927–1938.

Han, B., Mo, J., Kang, Z., and Zhang, F.Y. (2016). Effects of membrane electrode assembly properties on two-phase transport and performance in proton exchange membrane electrolyzer cells. Electrochim. Acta 188, 317–326.

Kadyk, T., Bruce, D., and Eikerling, M. (2016). How to Enhance Gas Removal from Porous Electrodes? Sci. Rep. 6, 1–14.

Kang, Z., Mo, J., Yang, G., Li, Y., Talley, D.A., Han, B., and Zhang, F.Y. (2017). Performance Modeling and Current Mapping of Proton Exchange Membrane Electrolyzer Cells with Novel Thin/Tunable Liquid/Gas Diffusion Layers. Electrochim. Acta 255, 405–416.

Kang, Z., Yang, G., Mo, J., Yu, S., Cullen, D.A., Retterer, S.T., Toops, T.J., Brady, M.P., Bender, G., Pivovar, B.S., Green, J.B., and Zhang, F.Y. (2018). Developing titanium micro/nano porous layers on planar thin/tunable LGDLs for high-efficiency hydrogen production. Int. J. Hydrogen Energy 43, 14618–14628.

Kim, P.J., Lee, C., Lee, J.K., Fahy, K.F., and Bazylak, A. (2020). In-Plane Transport in Water

Electrolyzer Porous Transport Layers with Through Pores. J. Electrochem. Soc. 167, 124522. https://doi.org/10.1149/1945-7111/abb173

Lee, C., Lee, J.K., Zhao, B., Fahy, K.F., and Bazylak, A. (2020). Transient Gas Distribution in Porous Transport Layers of Polymer Electrolyte Membrane Electrolyzers. J. Electrochem. Soc. 167, 024508. https://doi.org/10.1149/1945-7111/ab68c8

Lee, C.H., Hinebaugh, J., Banerjee, R., Chevalier, S., Abouatallah, R., Wang, R., and Bazylak, A. (2017). Influence of limiting throat and flow regime on oxygen bubble saturation of polymer electrolyte membrane electrolyzer porous transport layers. Int. J. Hydrogen Energy 42, 2724–2735.

Lee, C.H., Lee, J.K., Zhao, B., Fahy, K.F., LaManna, J.M., Baltic, E., Hussey, D.S., Jacobson, D.L., Schulz, V.P. and Bazylak, A. (2020). Temperature-dependent gas accumulation in polymer electrolyte membrane electrolyzer porous transport layers. J. Power Sources 446, 227312. https://doi.org/10.1016/j.jpowsour.2019.227312

Leonard, E., Shum, A.D., Danilovic, N., Capuano, C., Ayers, K.E., Pant, L.M., Weber, A.Z., Xiao, X., Parkinson, D.Y., and Zenyuk, I. V. (2020). Interfacial analysis of a PEM electrolyzer using X-ray computed tomography. Sustain. Energy Fuels 4, 921–931.

Leonard, E., Shum, A.D., Normile, S., Sabarirajan, D.C., Yared, D.G., Xiao, X., and Zenyuk, I. V. (2018). Operando X-ray tomography and sub-second radiography for characterizing transport in polymer electrolyte membrane electrolyzer. Electrochim. Acta 276, 424–433.

Lettenmeier, P., Kolb, S., Sata, N., Fallisch, A., Zielke, L., Thiele, S., Gago, A.S., and Friedrich, K.A. (2017). Comprehensive investigation of novel pore-graded gas diffusion layers for high-

performance and cost-effective proton exchange membrane electrolyzers. Energy Environ. Sci. 10, 2521–2533.

Lopata, J., Kang, Z., Young, J., Bender, G., Weidner, J.W., and Shimpalee, S. (2020). Effects of the Transport/Catalyst Layer Interface and Catalyst Loading on Mass and Charge Transport Phenomena in Polymer Electrolyte Membrane Water Electrolysis Devices. J. Electrochem. Soc. 167, 064507. https://doi.org/10.1149/1945-7111/ab7f87

Mazloomi, K., and Gomes, C. (2012). Hydrogen as an energy carrier: Prospects and challenges. Renew. Sustain. Energy Rev. 16, 3024–3033.

Sattari, E., Zanous, S.P., Farhadi, M., and Mohamad, A. (2020). Numerical investigation of the vapor bubble's scenarios passing through aerophobic/aerophilic porous structures using lattice Boltzmann method. J. Power Sources 454, 227929. https://doi.org/10.1016/j.jpowsour.2020.227929

Schuler, T., Ciccone, J.M., Krentscher, B., Marone, F., Peter, C., Schmidt, T.J., and Büchi, F.N. (2020). Hierarchically Structured Porous Transport Layers for Polymer Electrolyte Water Electrolysis. Adv. Energy Mater. 10, 1–12.

Schuler, T., Schmidt, T.J., and Büchi, F.N. (2019). Polymer Electrolyte Water Electrolysis: Correlating Performance and Porous Transport Layer Structure: Part II. Electrochemical Performance Analysis. J. Electrochem. Soc. 166, F555–F565.

Seweryn, J., Biesdorf, J., Schmidt, T.J., and Boillat, P. (2016). Communication—Neutron Radiography of the Water/Gas Distribution in the Porous Layers of an Operating Electrolyser. J. Electrochem. Soc. 163, F3009–F3011.

Suermann, M., Schmidt, T.J., and Buchi, F.N. (2015). Investigation of Mass Transport Losses in Polymer Electrolyte Electrolysis Cells. ECS Trans. 69, 1141–1148.

Suermann, M., Takanohashi, K., Lamibrac, A., Schmidt, T.J., and Büchi, F.N. (2017). Influence of Operating Conditions and Material Properties on the Mass Transport Losses of Polymer Electrolyte Water Electrolysis. J. Electrochem. Soc. 164, F973–F980.

Wang, J., Ji, L., Teng, X., Liu, Y., Guo, L., and Chen, Z. (2019). Decoupling half-reactions of electrolytic water splitting by integrating a polyaniline electrode. J. Mater. Chem. A 7, 13149–13153.

Zlobinski, M., Schuler, T., Büchi, F.N., Schmidt, T.J., and Boillat, P. (2020). Transient and Steady State Two-Phase Flow in Anodic Porous Transport Layer of Proton Exchange Membrane Water Electrolyzer. J. Electrochem. Soc. 167, 084509. https://doi.org/10.1149/1945-7111/ab8c89

LIST OF FIGURES

(C) 1 A/cm^2, 3 mlpm.
(D) 4 A/cm^2, 1 mlpm.
(E) 4 A/cm^2, 2 mlpm.
(F) 4 A/cm^2, 3 mlpm.

Figure 3. Oxygen content as a function of through-thickness PTL location
(A) The comparison of oxygen content at 1 A/cm^2 with varied water flow rates.
(B) The comparison of oxygen content at 4 A/cm^2 with varied flow rates.
(C) The comparison of oxygen content for varied current.

Figure 4. The comparison of oxygen content within the different portions of PTL at the operating condition of 1 A/cm^2, 2 mlpm
(A) (Top) 1/3 portions of PTL that located CL/PTL interface, Middle of PTL, and PTL/channel interface. (Bottom) 2D oxygen content of PTL at x-y plane by using Z-project method.
(B) Oxygen content comparison at different PTL portions.
(C) Z-project of the oxygen content of the x-z plane at the CL and PTL interface.
(D) Z-project of the oxygen content of the x-z plane at the middle PTL portion. (E) Z-project of the oxygen content of the x-z plane at the PTL and channel interface.

Figure 5. The comparison of oxygen content within the different portions of PTL at the operating condition of 4 A/cm^2, 2 mlpm
(A) (Top) 1/3 portions of PTL that located CL/PTL interface, Middle of PTL, and PTL/channel interface. (Bottom) 2D oxygen content of PTL at x-y plane by using Z-project method.
(B) Oxygen content comparison at different PTL portions.
(C) Z-project of the oxygen content of the x-z plane at the CL and PTL interface.
(D) Z-project of the oxygen content of the x-z plane at the middle PTL portion. (E) Z-project of the oxygen content of the x-z plane at the PTL and channel interface.

Figure 6. The comparison of oxygen content in the PTL between the CFD simulation and the experimental data at 1 and 4 A/cm^2 with water flowrate of 2 mlpm
(A) CFD simulation comparison with experimental results at the operating condition of 1 A/cm^2, 2 mlpm.
(B) CFD simulation comparison with experimental results at the operating condition of 4 A/cm^2, 2 mlpm.
(C) Average oxygen content for the three domains selected comparing CFD and experiment results for 1 A/cm^2.
(D) Average oxygen content for the three domains selected comparing CFD and experiment results for 4 A/cm^2 current densities.
(E-F) A conceptual schematic showing transport of oxygen in the PTL.

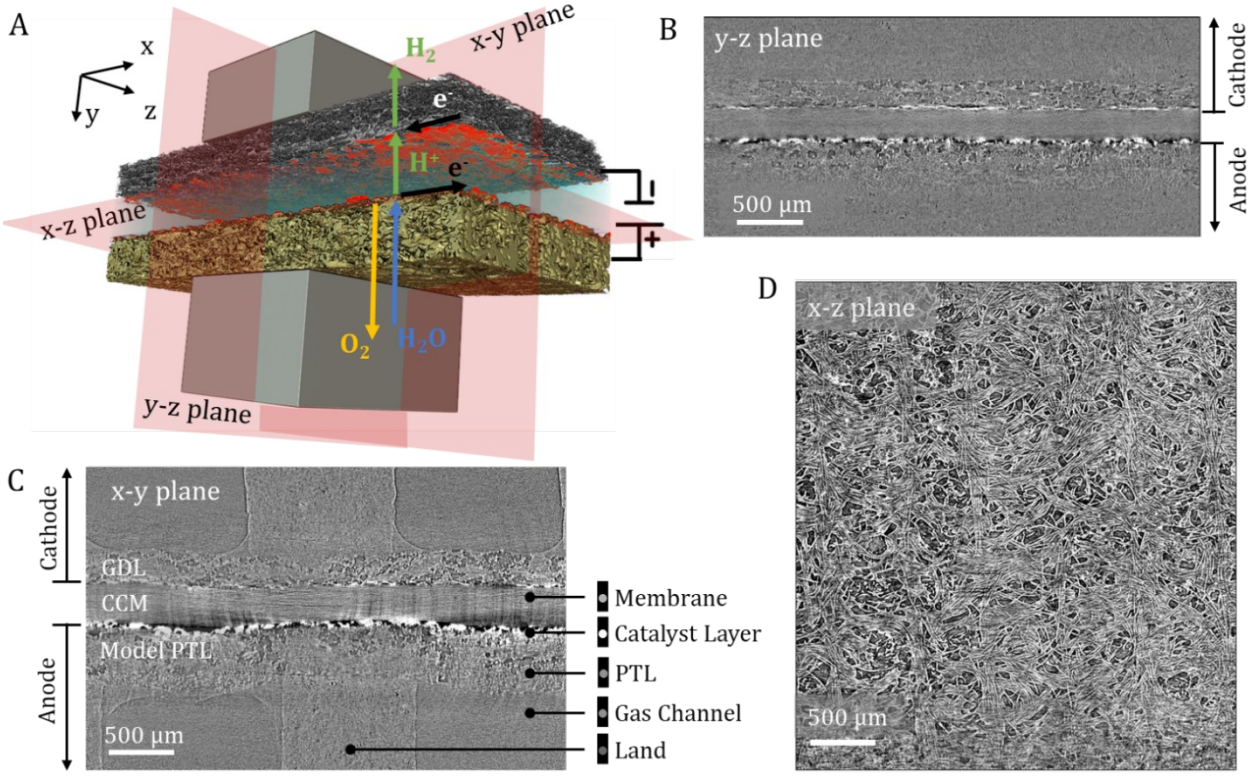

Figure 1. 3D volume rendering and the cross-section tomographs for the PEWE configuration

(A) 3D representation of a conventional PEWE obtained with x-ray CT, where the relevant viewing planes are highlighted, as well, as transport processes are shown. The treated Freudenberg GDL is on the bottom, and the carbon paper Freudenberg GDL is on the top.
(B) labeled cross-section of the x-y plane and detailing of electrolyzer components.
(C) labeled cross-sections of the y-z plane.
(D) labeled cross-sections of the x-z plane, where the Weka training was done on this plane.

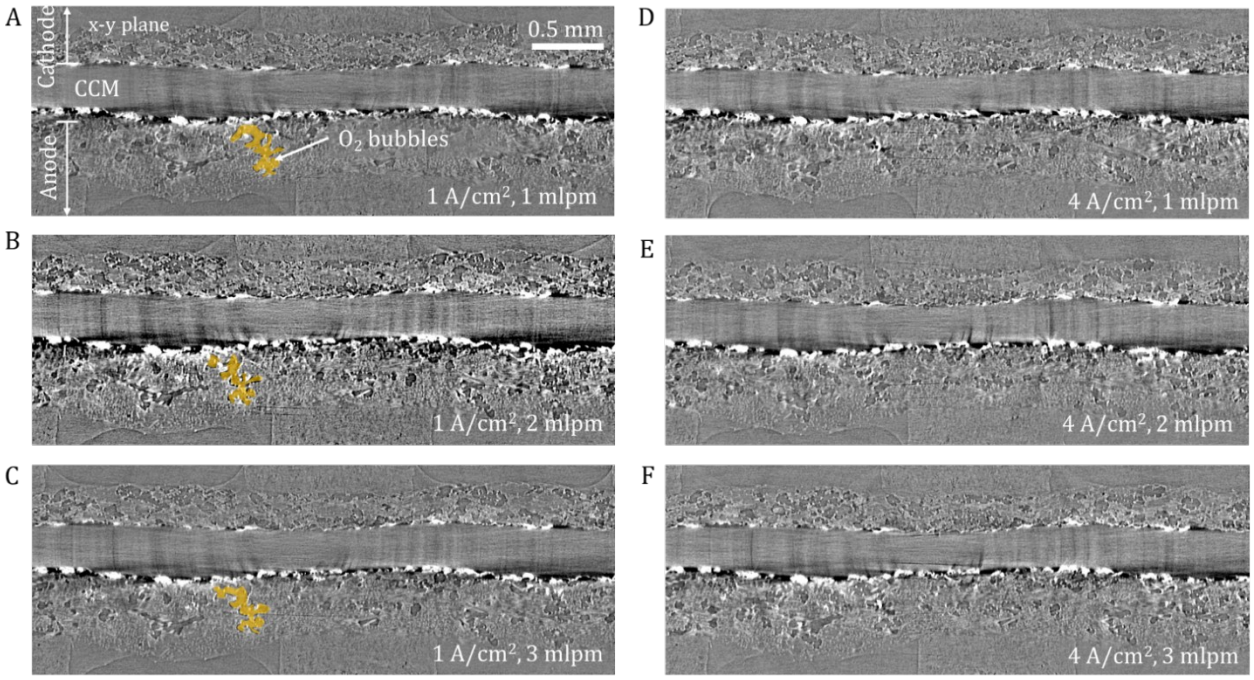

Figure 2. The x-y cross-section tomographs of the PEWE during cell operation, the cell temperature was 60°C

(A) 1 A/cm^2, 1 mlpm.
(B) 1 A/cm^2, 2 mlpm.
(C) 1 A/cm^2, 3 mlpm.
(D) 4 A/cm^2, 1 mlpm.
(E) 4 A/cm^2, 2 mlpm.
(F) 4 A/cm^2, 3 mlpm.

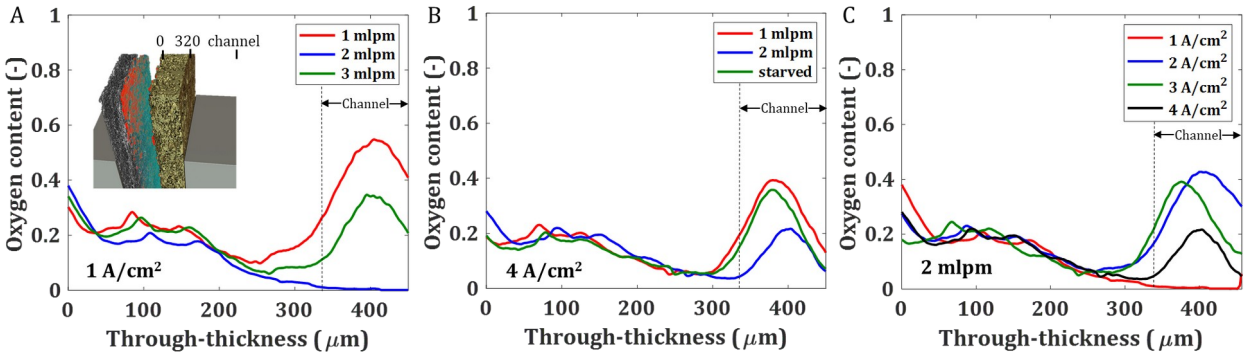

Figure 3. Oxygen content as a function of through-thickness PTL location
(A) The comparison of oxygen content at 1 A/cm^2 with varied water flow rates.
(B) The comparison of oxygen content at 4 A/cm^2 with varied flow rates.
(C) The comparison of oxygen content for varied current.

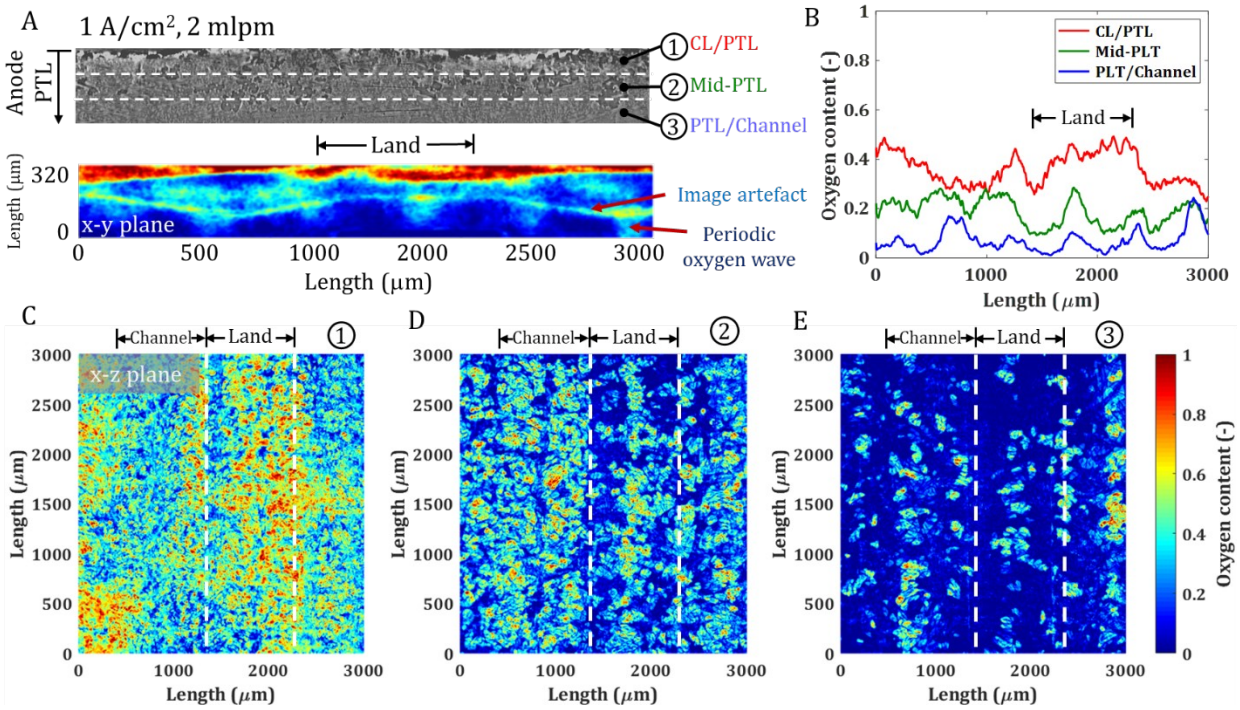

Figure 4. The comparison of oxygen content within the different portions of PTL at the operating condition of 1 A/cm², 2 mlpm

(A) (Top) 1/3 portions of PTL that located CL/PTL interface, Middle of PTL, and PTL/channel interface. (Bottom) 2D oxygen content of PTL at x-y plane by using Z-project method.
(B) Oxygen content comparison at different PTL portions.
(C) Z-project of the oxygen content of the x-z plane at the CL and PTL interface.
(D) Z-project of the oxygen content of the x-z plane at the middle PTL portion. (E) Z-project of the oxygen content of the x-z plane at the PTL and channel interface.

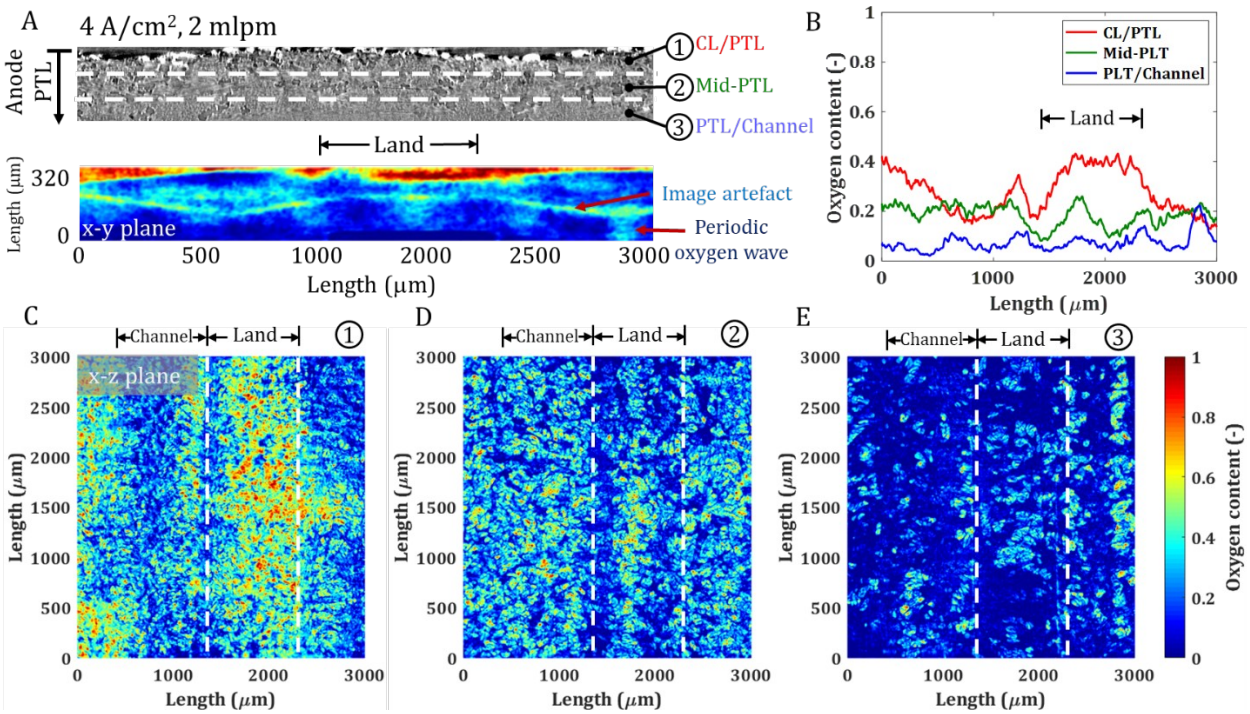

Figure 5. The comparison of oxygen content within the different portions of PTL at the operating condition of 4 A/cm², 2 mlpm

(A) (Top) 1/3 portions of PTL that located CL/PTL interface, Middle of PTL, and PTL/channel interface. (Bottom) 2D oxygen content of PTL at x-y plane by using Z-project method.

(B) Oxygen content comparison at different PTL portions.

(C) Z-project of the oxygen content of the x-z plane at the CL and PTL interface.

(D) Z-project of the oxygen content of the x-z plane at the middle PTL portion. (E) Z-project of the oxygen content of the x-z plane at the PTL and channel interface.

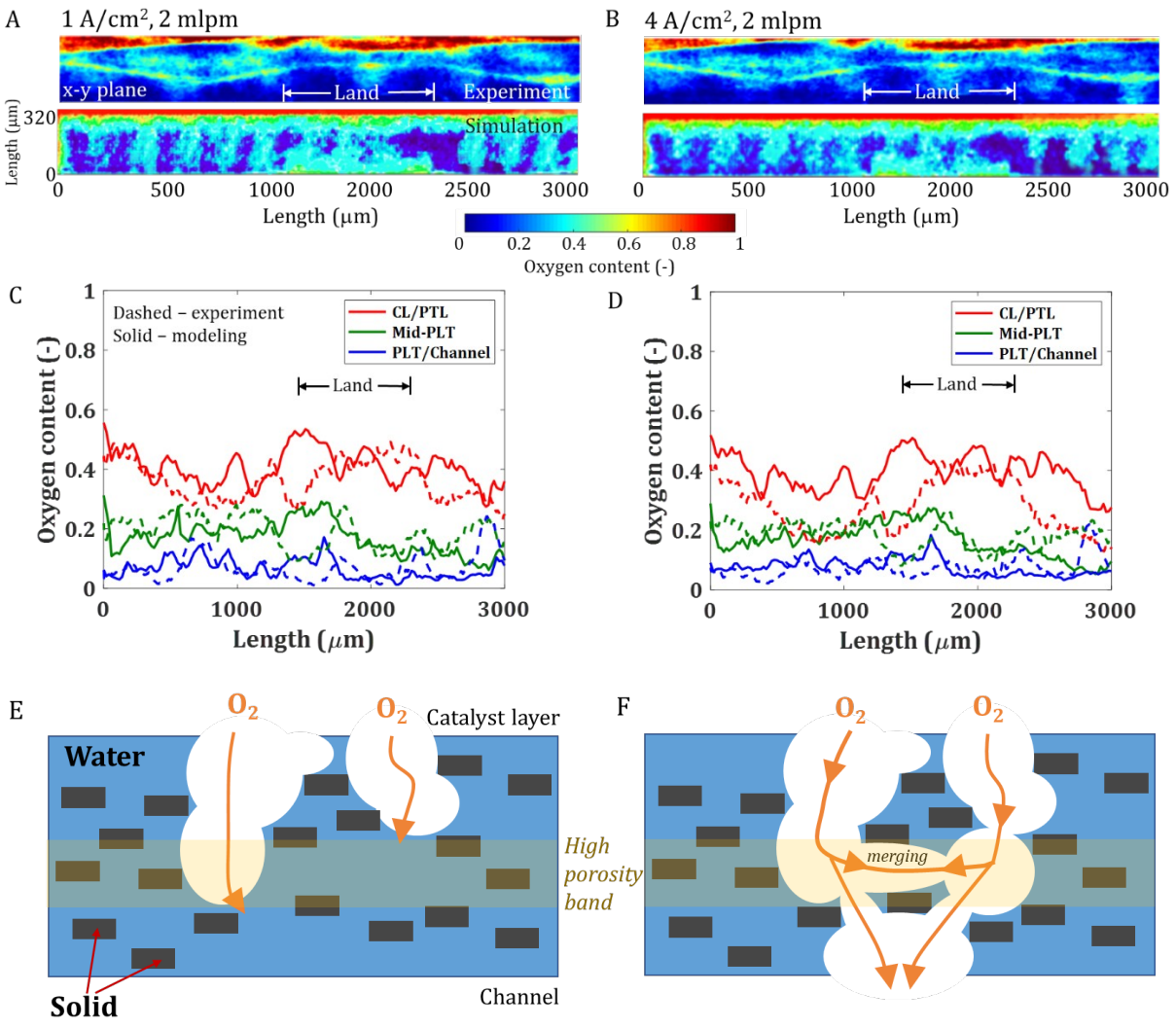

Figure 6. The comparison of oxygen content in the PTL between the CFD simulation and the experimental data at 1 and 4 A/cm² with water flowrate of 2 mlpm

(A) CFD simulation comparison with experimental results at the operating condition of 1 A/cm², 2 mlpm.

(B) CFD simulation comparison with experimental results at the operating condition of 4 A/cm², 2 mlpm.

(C) Average oxygen content for the three domains selected comparing CFD and experiment results for 1 A/cm².

(D) Average oxygen content for the three domains selected comparing CFD and experiment results for 4 A/cm² current densities.

(E-F) A conceptual schematic showing transport of oxygen in the PTL.